Cruise Propulsion System Thermal Analysis for NASA's X-57 "Maxwell" Mod II Configuration

Nicholas K. Borer[1]
NASA Langley Research Center, Hampton, Virginia, 23681, USA

Trong Bui[2]
NASA Armstrong Flight Research Center, Edwards, California, 93523, USA

Andrew D. Smith[3]
NASA Glenn Research Center, Cleveland, Ohio, 44135, USA

The X-57 "Maxwell" is NASA's flight demonstrator for distributed electric propulsion technologies. The X-57 Mod II configuration is designed to test the electric cruise propulsion system for X-57 and features an electric cruise motor mounted in an integral nacelle on each wing. The electric motors and associated control equipment for X-57 Mod II are air-cooled; therefore, they require adequate cooling airflow to stay within temperature limits set by the X-57 project in all relevant flight conditions. A computational flow analysis was conducted to estimate the internal flow properties of the X-57 Mod II cruise nacelles in three critical flight conditions. These flow properties were then used to determine the boundary conditions for individual component thermal models, which were used to estimate individual component operating temperatures. The results indicated that the low-speed, low-altitude initial takeoff climb during hot day conditions was the sizing condition from a cooling perspective. The analysis found that the cooling flowpaths in the X-57 Mod II cruise nacelles are adequate to provide cooling to most of the components with the appropriate amount of thermal margin. The two components that are not anticipated to have the appropriate margin can be accommodated with a small (< 2°C) adjustment to the project operating limitations.

I. Introduction

The National Aeronautics and Space Administration (NASA) is developing the X-57 Maxwell, a research aircraft that will serve as a flight demonstrator for Distributed Electric Propulsion (DEP) technology [1]. The X-57 is demonstrating this technology through successive retrofits, called "Mods" (for "modifications"). The sequence of these Mods is given in Fig. 1, which shows the evolution of the aircraft from a general aviation baseline in Mod I to a fully distributed electric propulsion flight demonstrator in Mod IV.

The X-57 uses two electric cruise propulsion units in the Mod II, III, and IV configurations. The cruise propulsion hardware other than the propeller (i.e., the motor, motor controller, and associated power and data systems) is located in two cruise nacelles. The purpose of these nacelles is to reduce the aerodynamic drag of these components by directing air around them and to provide airflow through the nacelle to help manage the temperature of these components during operation. In Mod II, the cruise nacelles are located on the inboard sections of the aircraft wing, more or less in the same location as the nacelles on the original donor aircraft. The nacelle geometry has been modified

[1] Performance and Sizing Team Lead, Aeronautics Systems Analysis Branch, AIAA Associate Fellow.
[2] Aerodynamics and Propulsion Branch, AIAA Senior Member.
[3] Thermal Systems and Transport Processes Branch, nonmember.

from the original aircraft to fit the new electric propulsion components and to create the appropriate flowpaths to help manage the thermal loads of these components. For the Mod III and IV configurations, the cruise motors and associated equipment are in wingtip-mounted nacelles. The Mod II and Mod III/IV arrangements are shown in Fig. 2.

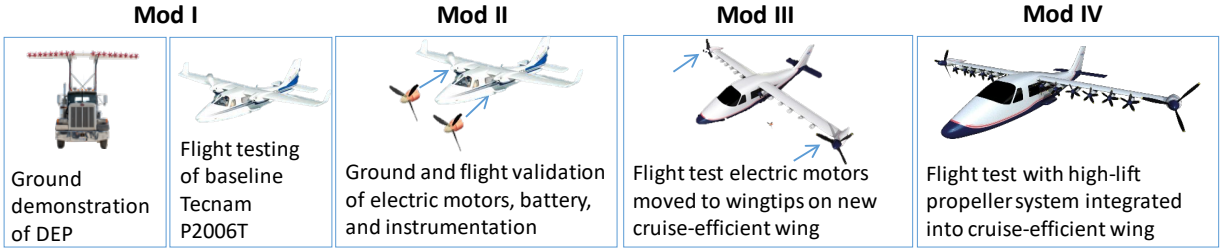

Fig. 1 X-57 development through multiple modifications ("Mods").

Fig. 2 Picture of the X-57 in the Mod II configuration with cruise propellers mounted on inboard nacelles (left), and a rendering of the X-57 in the Mod III/IV configuration with cruise propellers mounted on wingtip-mounted nacelles (right).

The X-57 cruise propulsion system components rely on airflow, rather than a dedicated cooling system, to passively dissipate the heat generated during operation. Many of these components include heat sinks or other features to move waste heat to moving air and transfer the heat out of the components. The X-57 cruise nacelle design in both Mod II and Mod III/IV, therefore, needs to provide adequate airflow to these components during all expected operations, ensuring that the component temperatures remain within operating limits.

This paper describes the analysis approach and component temperature estimates associated with operation of the cruise propulsion system components within the nacelles of the X-57 Mod II configuration. This includes a description of the driving conditions, a description of the computational fluid dynamics (CFD) model used to model the airflow around and through the Mod II nacelle, and an estimate of component temperatures in these driving conditions when the CFD airflow estimates are coupled with a thermal model of the cruise propulsion system components.

II. Cooling System Requirements

The X-57 cooling requirements are derived from a subsystem requirement which states, "[The] values for the cooling system for the cruise and high-lift motors and controllers shall be able to operate at maximum continuous power throughout the relevant areas of the flight envelope." This requirement was established to ensure that the aircraft could sustain flight during climb conditions at Maximum Continuous Power (MCP). Three characteristics emerge from this statement:

1) the cooling requirements apply to the cruise and high-lift motors and controllers,*
2) the components cannot exceed temperature limits that could cause them to cease operation at a specified power level (MCP), and
3) adequate cooling is necessary in "relevant areas of the flight envelope," implying that the type of operation should be considered when selecting sizing flight conditions for system thermal characteristics.

A. Cruise Propulsion System Component Thermal Models and Component Temperature Limits

The X-57 cruise nacelle contains multiple active electrical components that generate waste heat and are sensitive to high temperatures. These components are captured in the Integrated Cruise Propulsion Thermal (ICPT) model, which is a collection of metamodels built from higher-fidelity thermal models, augmented with test data for many of the individual components. The ICPT integrates thermal models of the Cruise Motor (CM), Cruise Motor Controllers (CMCs), Miniaturized Data Acquisition Unit (MDAU), and Fiber Optic Bus Extender (FOBE). The CMCs include a heat sink for heat dissipation from the high-voltage Field Effect Transistors (FETs) on one side of the CMC case, and for the low-voltage components, such as the driver board, Alternating Current-to-Direct Current (AC/DC) board, Field Programmable Gate Array (FPGA) board, and Central Processing Unit (CPU) board, on the opposite side. Most importantly, the ICPT model requires flow conditions for local air temperature, mass flow rate or velocity (depending on the component model), and power dissipation. The component temperature limits are largely prescribed by manufacturer-provided data sheets, applicable rating/de-rating factors, and a project-specified thermal margin allocation. The component temperature limits and associated margined limits are shown in Table 1. A two-dimensional slice of the nacelle is shown in Fig. 3 that indicates the location of critical components.

Table 1 Maximum allowable component temperatures for electronic components in the cruise nacelles

Component	Limit (°C)	Margined Limit (°C)
CM (aft) winding (high voltage) temperature	135	124
CM magnet temperature	94	83
CMC FET junction temperature (high voltage)	175	150
CMC FPGA temperature (low voltage)	100	89
CMC driver board temperature (low voltage)	100	89
CMC AC/DC board temperature (low voltage)	85	74
CMC CPU board temperature (low voltage)	85	74
MDAU case temperature	85	74
FOBE case temperature	85	74

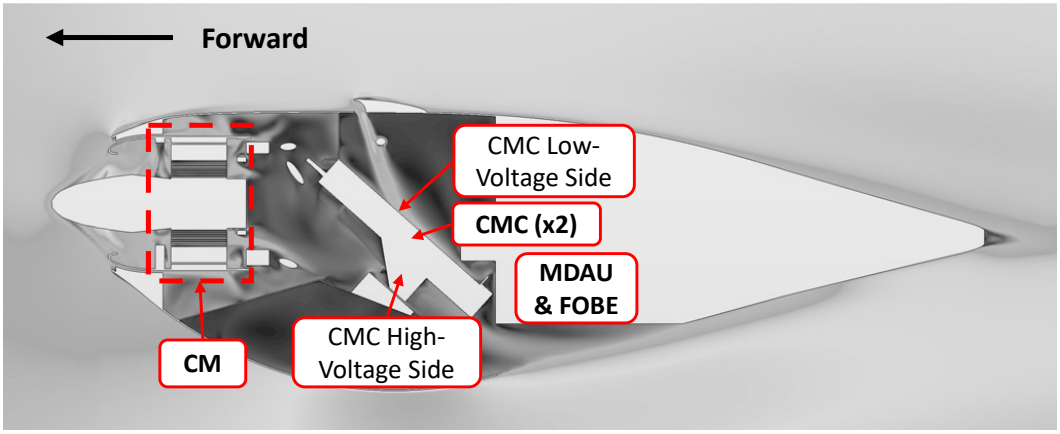

Fig. 3 Section of Mod II cruise nacelle illustrating location of critical components.

* The scope of this paper is related to the thermal analysis cruise propulsion system since the Mod II configuration does not use high-lift motors.

B. Operating Conditions

The project subsystem requirement for thermal characteristics indicates that cooling shall be evaluated at a specified power level but necessitates the engineering team determine relevant operating areas of the flight envelope. The subsystem requirement applies only to operation at maximum continuous power, but the cases where the aircraft is expected to operate at peak power (i.e., during takeoff and initial climb) are also considered in this document.

Ambient conditions are an important factor for thermal analysis. The temperature difference between the environment and the component heat sink has a significant impact on the amount of heat energy that can be dissipated. The team developed reference atmospheres for performance characterization based on the X-57 test site at the Dryden Aeronautical Test Range in Edwards, California. The X-57 Project Hot Day Reference Atmosphere provided the most stringent thermal reference conditions and, therefore, sets the ambient conditions for the analysis in this document. These conditions, shown in Table 2, were derived from climatology data at Edwards Air Force Base [2].

Table 2 X-57 Project Hot Day Reference Atmosphere

Pressure altitude, ft	Temperature, °R	Pressure, lb_f/ft^2	Density, $slug/ft^3$	Speed of sound, ft/s	Viscosity, slug/ft-s
0.0	565.98	2116.2	0.0021787	1166.1	4.0531×10^{-7}
1635.7	560.07	1994.0	0.0020746	1160.0	4.0201×10^{-7}
2288.9	557.48	1946.9	0.0020349	1157.3	4.0056×10^{-7}
3174.2	552.43	1884.4	0.0019876	1152.1	3.9773×10^{-7}
4759.6	547.60	1776.5	0.0018904	1147.0	3.9500×10^{-7}
6345.6	541.07	1673.7	0.0018025	1140.2	3.9131×10^{-7}
7930.2	533.91	1575.9	0.0017199	1132.6	3.8723×10^{-7}
9510.6	526.76	1482.9	0.0016404	1125.0	3.8313×10^{-7}
11091.5	520.01	1394.5	0.0015626	1117.8	3.7923×10^{-7}
12673.0	513.44	1310.3	0.0014870	1110.7	3.7542×10^{-7}
14251.5	507.14	1230.4	0.0014138	1103.8	3.7174×10^{-7}
15831.9	500.97	1154.5	0.0013428	1097.1	3.6812×10^{-7}
17413.1	494.75	1082.3	0.0012747	1090.3	3.6444×10^{-7}

Three driving steady-state flight conditions were identified – **initial takeoff climb**, **cruise climb**, and **dash**. A summary of these conditions is given in Table 3, and the rationale for the values selected for each of these conditions is expanded upon in the sections below. This table refers to pressure altitude (h_p), airspeed (V), and ambient temperature (T).

Table 3 Steady-State flight conditions analyzed in this document

Flight Condition	h_p (ft)	V (KEAS/KTAS)	T (°C/°F)	Power Setting[†]
Initial Takeoff climb	2,500	70 / 76	35.9 / 96.6	Peak (72.1 kW)
Cruise climb	2,500	81 / 88	35.9 / 96.6	MCP (60.0 kW)
Dash	8,000	128 / 150	23.3 / 73.9	Peak (72.1 kW)

1. Initial takeoff climb

The initial takeoff climb flight condition represents the phase after the aircraft has lifted off and has reached the initial climb speed with takeoff power set. In the takeoff configuration, the flaps are in the takeoff position and landing gear is down, which significantly increases the drag and decreases the climb rate. To maintain an adequate climb rate, it is desired to operate at slower airspeeds (to minimize the impact of the increased parasite drag) and higher power settings (to provide more thrust). The former consideration limits cooling by reducing airflow to remove waste heat, and the latter increases heat loads since the aircraft will be operating at a higher power setting than MCP. The driving flight conditions were set by the lowest airspeed allowable (in this case at the best angle of climb speed), while operating at the highest permissible power setting (in this case peak power, 72.1 kW of shaft power), and at the highest ambient temperature. Since the pressure altitude will change with ambient conditions and the initial climb configuration is maintained until 500 ft of altitude above ground level, the team chose 2,500 ft of pressure altitude (approximately 200 ft above Edwards field elevation at standard pressure) to set the ambient conditions. Finally, the other parameters were set to the X-57 Project Hot Day reference atmosphere.

[†] Power setting is referenced to motor shaft power.

2. Cruise climb

The cruise climb flight condition represents the flight phase after the aircraft is reconfigured at the completion of the initial climb. In this phase, the flaps are retracted to the cruise position and the landing gear is retracted. The airspeed is increased, and the power is reduced from peak to MCP, both of which will improve cooling. For this flight condition, the atmospheric parameters of the initial takeoff climb condition were used, even though the hottest ambient conditions would likely be experienced at 2,800 ft pressure altitude. The difference is small enough that the initial climb atmospheric condition at 2,500 ft pressure altitude was maintained, which allows direct comparison between the initial takeoff climb and cruise climb values.

3. Dash

The dash flight condition represents a power setting at higher altitude used for completion of some of the flight maneuvers in the test plan. The project design driver includes comparison of energy consumption between the original aircraft and Mods II-IV at 8,000 ft mean sea level and 150 knots true airspeed (KTAS). The Mod II aircraft will likely require greater than MCP to reach this condition. Dash was evaluated in the cruise configuration at peak power, 150 knots KTAS, and 8,000 ft pressure altitude. On a hot day, this equates to 128 knots equivalent airspeed (KEAS).

C. Heat Loads

The operating conditions above include operation of the cruise propulsion system at specified power settings but do not directly address the heat loads from the components. These heat loads are based on estimates from known data sheets for the low-voltage components and from limited modeling and testing conducted with the CM and CMC for the high-voltage components.

A summary of the heat loads used in this analysis is given in Table 4. Dynamometer testing can be used to determine motor and controller losses but not to determine how much of those losses should be apportioned to the stator windings versus the rotor magnets. The team used models and test data to determine the portion of heat loads for the CM stator versus CM rotor. The analysis indicated that the stator loads were responsible for 90% of the losses, and those loads were evenly distributed over the surface area of the stator windings. The other 10% was applied to the magnets.[‡] The CM is an outrunner motor, meaning the outer portion of the motor is the rotor. Half of the magnet heat is rejected over the outer portion of the rotor and the other half is concentrated towards the interior flowpath, which also serves to cool the stator. The distribution of heat loads in other components is more straightforward; the waste heat from the CMC FETs is distributed to the heat sink fins on the high-voltage side of the CMCs, and the entire backplate of the CMC is used as the heat sink for the low-voltage components. Since the MDAU and FOBE are in an area of the X-57 Mod II nacelle that is not in the same flowpath as the CM and CMCs, these components were not modeled as part of the CFD analysis but were tracked in the ICPT.

Table 4 Heat loads used for analyses

Component	Heat (W)	Efficiency	Distribution Notes
CM stator windings @ peak power	5,237	92.53% (combined)	90% of motor losses from dyno test
CM rotor magnets @ peak power	582		10% of motor losses from dyno test, 50% to outer portion of motor
CMC high-voltage heat sink @ peak power (each)	810	97.96%	Applied to heat sink fins
CM stator windings @ MCP	4,196	92.80% (combined)	90% of motor losses from dyno test
CM rotor magnets @ MCP	466		10% of motor losses from dyno test, 50% to outer portion of motor
CMC high-voltage heat sink @ MCP (each)	679	97.95%	Applied to heat sink fins
CMC low-voltage heat sink (each)	30	N/A	Applied to CMC backplate
MDAU	8	N/A	Only used in ICPT model, not CFD
FOBE	3	N/A	Only used in ICPT model, not CFD

[‡]Some of the motor losses could be applied to the bearings, but the bearing heating and loads were considered separately as part of the motor design, and the bearings are not exposed to any meaningful airflow in the nacelle.

III. Modeling Approach

A CFD model was used to simulate the full three-dimensional air flow inside the cruise motor nacelle. This model included all relevant motor components inside the cruise motor nacelle as well as the external freestream and the flow induced by the propeller. The SimCenter STAR-CCM+ package was used for the CFD solver [3]. The internal nacelle air flow properties obtained from the CFD analysis were passed to the ICPT model. The resulting component temperatures from the ICPT model were then compared against the established component temperature limits from Table 1 to determine if the analyzed motor nacelle configuration satisfies the thermal requirements for the aircraft and cruise motor operating conditions under consideration.

A. Geometry for CFD Analysis

To make the CFD analysis tractable with limited computational resources, the team analyzed an isolated motor pod in free air without the rest of the X-57 airplane and wing. The CFD model included relevant motor nacelle components including the propeller disc, the spinner, the motor nacelle's outer mold lines, and the internal components. Both external and internal flows, including the propeller-induced flows, were modeled. In addition to influencing the flows on the outside of the nacelle, the propeller also induces flows into the motor nacelle through the annulus between the prop spinner and the motor nacelle, as well as into the two cooling air scoops on top of the motor nacelle. These air scoops (located directly above the CMCs) are required to provide cooling air for the low-voltage CMC electronics. The CM stator, CM rotor, CMC, and CMC high-voltage heat sink fins were included in the Mod II CFD model. This model also included all critical flow baffles and ducting internal to the motor nacelle, as well as major structural struts/braces. All internal volumes aft of the motor compartment were treated as dead space and not modeled. The cruise propeller was modeled using a body force virtual disk approach.

B. CFD Setup and Gridding

A fully viscous Navier-Stokes 3D CFD model was used. The internal flow is likely to be turbulent due to the complex and circuitous flow paths inside the motor nacelle, swirling flows due to rotating hardware components, and the large amount of heat transfer. Therefore, a steady non-transient CFD model was used, and the Shear Stress Transport (SST) k-ω turbulence model [4,5] was used for all CFD simulations. This was a conservative assumption consistent with the equilibrium assumption in the ICPT model, since the CFD solution provides the air temperatures after being heated for a long time following the initial heating transient. The CFD model included rotating and stationary motor components, as well as all relevant physics such as propeller-induced flow, heat addition from motor components, air conduction and convection heat transfer, and hot air buoyancy. The rotating hardware components were modeled by prescribing the rotational wall velocities on the surfaces of these components as part of the boundary conditions for the CFD simulations. Given a set of aircraft and motor operating conditions, the CFD solution provided a complete description of internal and external nacelle air mass flow rates, velocities, temperatures, and pressures.

An unstructured CFD grid was used due to the complex geometries inside the cruise motor nacelle as well as the requirement to rapidly iterate changes in the motor nacelle's hardware configuration for design purposes. The flows both inside and outside of the nacelle were discretized into finite volume cube-shaped CFD cells, which were then subdivided into smaller cubes to refine the volume cells in complex flow areas. A vertical cut plane visualization through the middle of the motor nacelle's CFD grid volume is shown in Fig. 4. The grid is much finer inside the motor nacelle and the propeller virtual disk to resolve the complex flows in these regions; then, the grid coarsened further out into the uniform freestream flow. The white area in the aft compartment of the nacelle (Fig. 4) was modeled as an empty space with no flowpaths or heat transfer in the CFD model.[§]

Details of the CFD grid by the surfaces of major electric motor components are shown in Fig. 5. Both the nacelle's outer skin and the various flow baffles have been removed in this picture to show the major motor hardware components including the propeller spinner, the motor stator with its cooling slots, the rotor-stator gap, the rotor, the motor mount, the CMC with major electrical connectors, the CMC cooling fins, and the baffles around the CMC cooling fins. The baffles are needed to direct the air flows through the CMC cooling fins.

The CFD model could not be experimentally validated due to the lack of air flow test data for the Mod II cruise motor nacelle. The CFD grid sizes for the various components in the model were carefully selected from a grid independence study for a Mod III cruise motor nacelle CFD model, which utilizes the same motor components. The results of this grid independence study showed that grid sizes considered credible for this study did not result in significant variations.

[§] This area does hold some heat-generating equipment including data acquisition and communication hardware; however, the heat was assumed to have no effect on the upstream components and is not included in the CFD model.

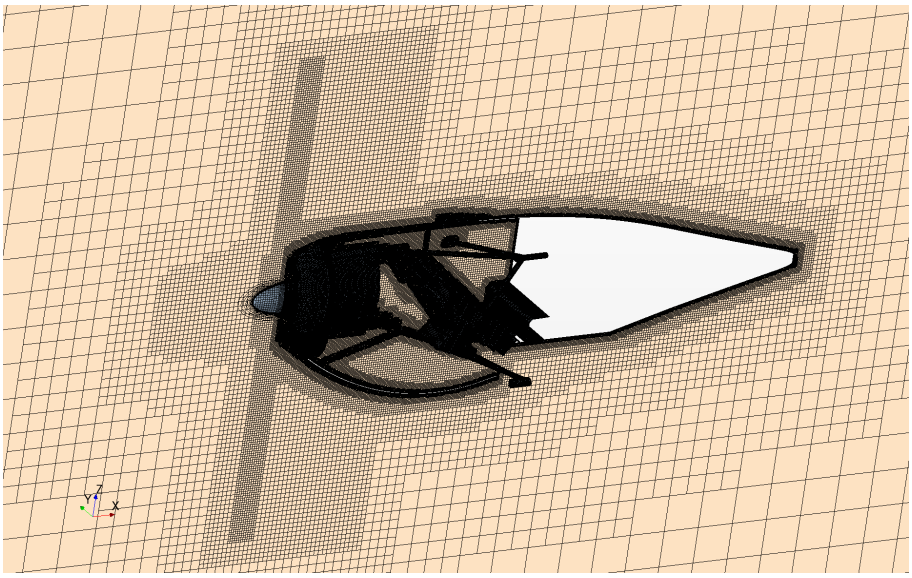

Fig. 4 Volume mesh on a cut plane through the computational domain for the Mod II cruise nacelle.

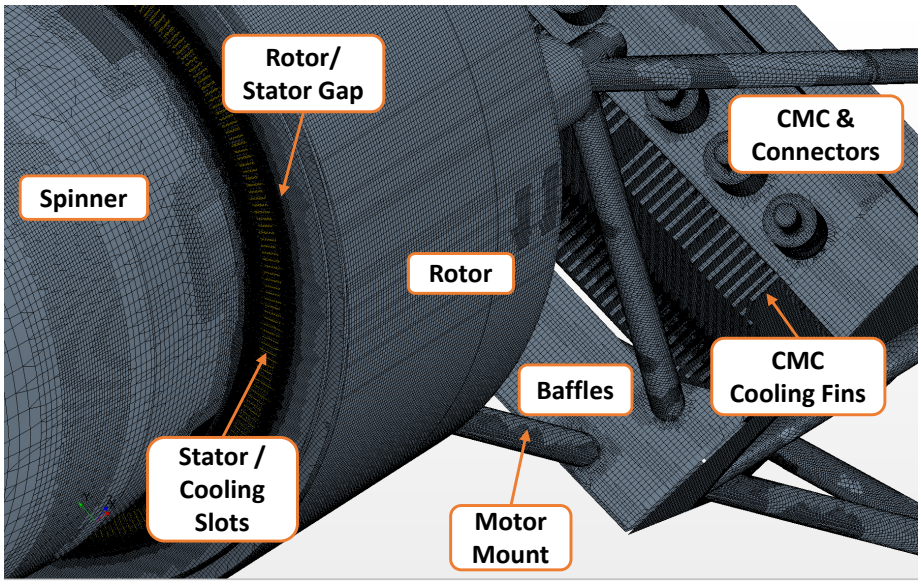

Fig. 5 Surface mesh details on major components inside the Mod II cruise nacelle (nacelle skins and baffles are removed for visualization purposes).

IV.Model Results

The CFD model was analyzed for each of the three flight conditions described previously in Table 3 along with the corresponding heat loads from Table 4. The detailed flow station results, including definitions of the flow stations, are given in the Appendix. A summary of the results follows below.

A. Nacelle Flowpaths

A 2-D cross-section of the nacelle is shown in Fig. 6. This cross-section is a slice slightly off the centerline through one of the two inlets on the top of the nacelle. This off-center slice was used to capture flow details through one of the two upper inlets in the Mod II nacelle. The same cross-section given in Fig. 7 depicts different flow paths and shows the complex cooling and mixing regions that are common throughout the different flight conditions.

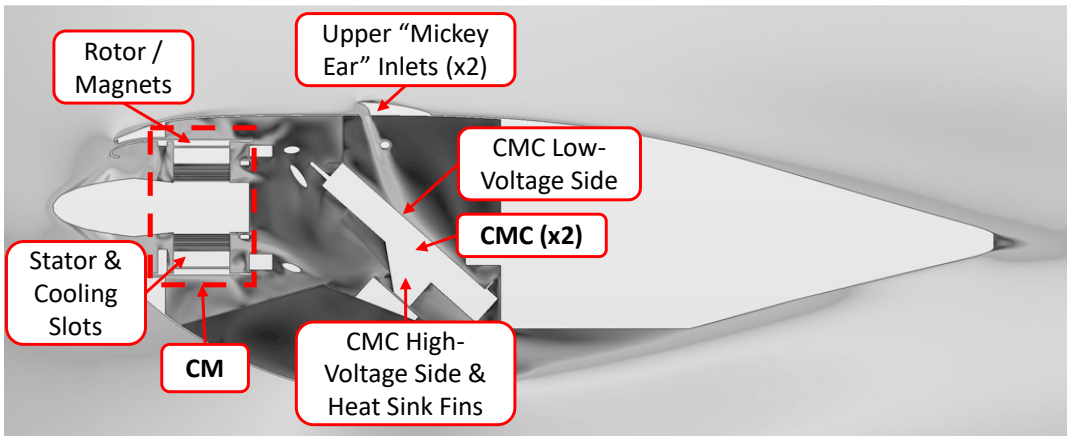

Fig. 6 Section of Mod II cruise nacelle illustrating location of critical components for thermal/CFD analysis.

Starting from the left in Fig. 7, the airflow enters the front of the nacelle in one of two regions –between the propeller spinner and inside "lip" of the CM, or between the outer "lip" of the CM and the nacelle. These are known as the **CM cooling** flow and the **CM bypass** flow, respectively. The **CM cooling** flow passes between the rotor-stator gap and provides cooling airflow to the CM stator windings as well as the lower portion of the CM rotor magnets. As seen earlier in Table 4, the stator windings represent the highest heat loads in the nacelle. The CM bypass flow cools the outside of the CM rotor. Here, the only heat load is located in the upper portion of the CM magnets.

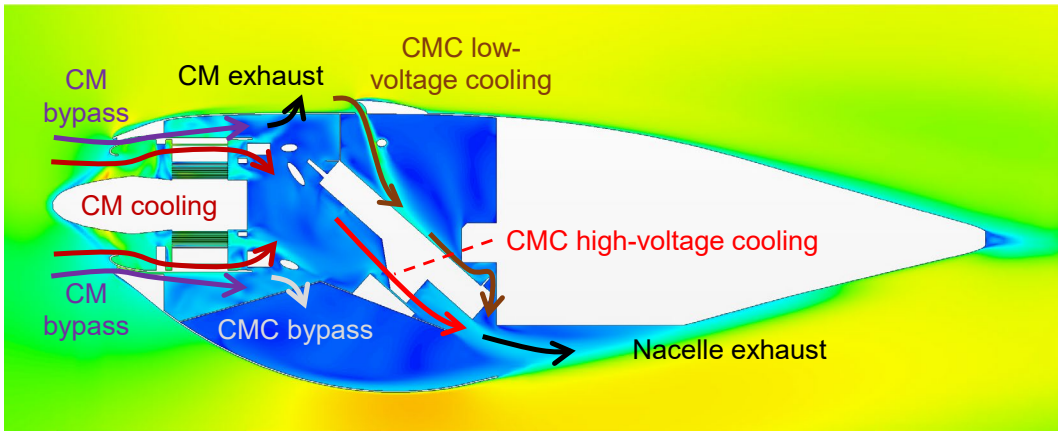

Fig. 7 Section of Mod II cruise nacelle illustrating interaction of different cooling flows.

The **CM bypass** flow and **CM cooling** flow mix behind the CM and ahead of the CMC. To reduce backpressure in this area and promote more flow through the CM, a louvered vent was added in the top center of the nacelle forward of the CMC mounting bulkhead to exhaust some of this hot air as depicted in the **CM exhaust** flow. Additionally, some of the mixed **CM bypass** and **CM cooling** flow goes through an opening in a plenum that separates the CM from the lower portion of the cowl to further reduce the backpressure aft of the CM as depicted in the **CMC bypass** flow. The air that is not exhausted or bypassed is directed to pass through the CMC high-voltage heat sinks in the **CMC high-voltage cooling** flow. This illustrates the tradeoff involved in CM vs. CMC cooling – increasing **CM bypass** flow increases the **CMC high-voltage cooling** flow but decreases the **CM cooling** flow.

The back plate of the CMC is used as a heat-sink for the low-voltage electronics. Since these components tend to have a lower overall temperature limit, cooling air is brought from the ambient air through the two small inlet scoops on the top of the nacelle. These "Mickey Ear" inlets get their name from their half-moon shape and the fact that they are spaced such that they will not ingest hotter air exiting from the **CM exhaust** flow. Each scoop provides a jet of cool outside air to the back of each CMC, which then exits this space along the bottom edge of the CMCs, as depicted in the **CMC low-voltage cooling** flow. The **CMC bypass** flow, **CMC high-voltage cooling** flow, and **CMC low-voltage cooling** flow mix and exit the nacelle through the lower exhaust as depicted in the **nacelle exhaust** flow.

B. Nacelle Flow Velocity and Temperature Estimates

Of all the flight conditions, the initial takeoff climb is the most constraining since the aircraft is moving at the slowest airspeed while the CM and CMC are giving off their largest heat loads. A 2-D cross-section of the nacelle is shown in Fig. 8 with contours colored by velocity magnitude for the initial takeoff climb case. The same flight condition is shown in Fig. 9, but with contours colored by air temperature. The detailed results at selected flow stations, including pressure, temperature, velocity, and mass flow rate, are provided in the Appendix.

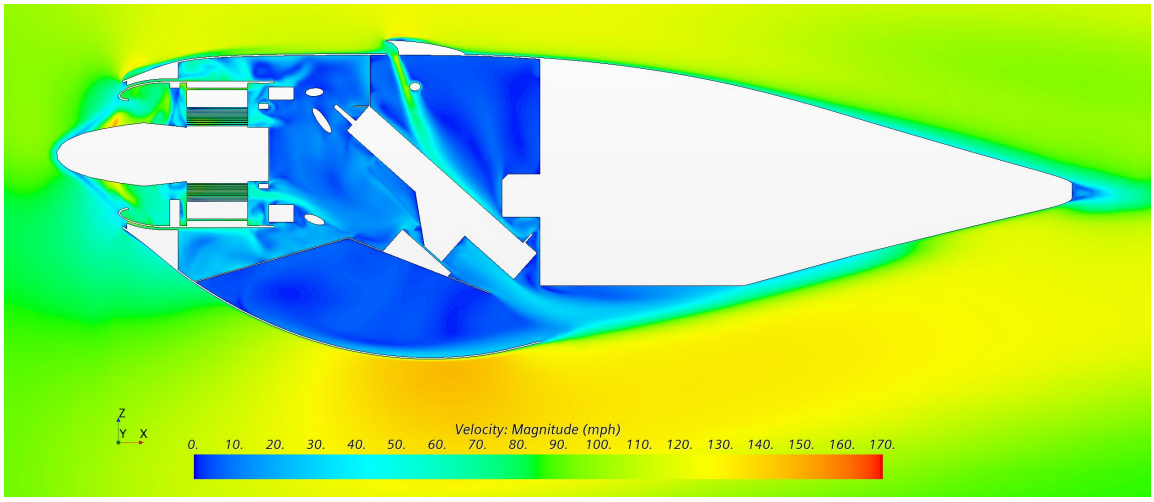

Fig. 8 Air velocity contours in the Mod II cruise nacelle for the initial takeoff climb flight condition.

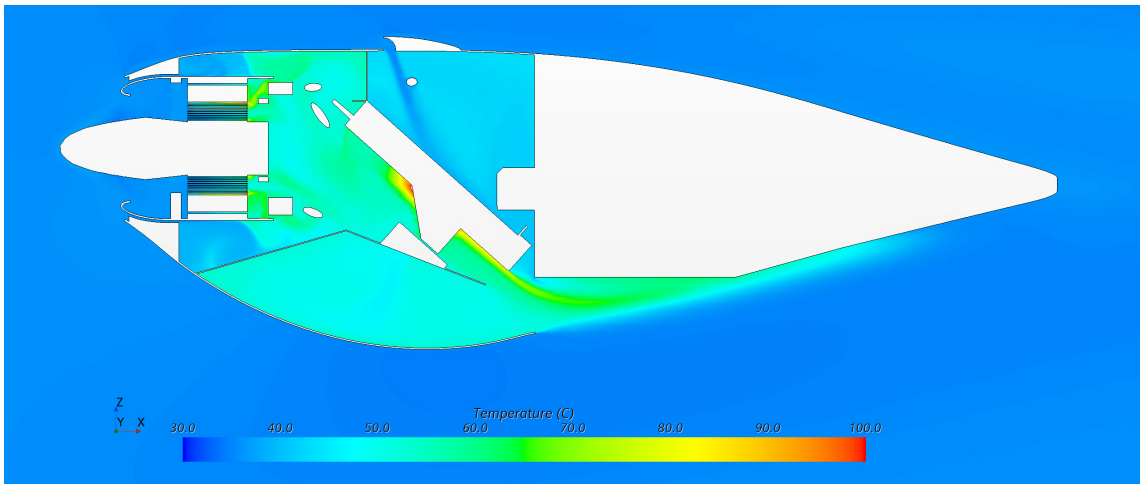

Fig. 9 Air temperature contours in the Mod II cruise nacelle for the initial takeoff climb flight condition.

The highest internal average air temperature occurs at the exit of the motor cooling slots in the **CM cooling** flow, reaching 67.2°C. Like the other flow properties, the temperatures given in the Appendix are averaged over the entire cross section of the flow, so there are regions of the flow with higher temperatures. For example, in Fig. 9, it appears that a small region prior to the CMC high-voltage heat sink approaches 100°C. The flow station value used to analyze the performance of the high-voltage heat sink is averaged over a cross-section that is approximately the height of the CMC heat sink fins as detailed in Fig. 14 (in the Appendix), which is why the value used in the analysis is 67.2°C. The second highest internal average temperature in the flow path is at the exit of the **CMC high-voltage cooling** flow, reaching 62.1°C. The maximum average temperature for the **CMC low-voltage cooling** flow is 46.7°C.

The cruise climb flight condition is less constraining than initial takeoff climb but represents the flight condition where X-57 will spend a sizable portion of the mission – climbing at cruise climb speeds at MCP to reach an altitude for flight test points. Here, the airspeed is higher and the overall power levels are lower than the initial takeoff climb, resulting in higher air velocities, higher mass flows, and lower steady-state temperatures inside the nacelle. Two-dimensional slices of the velocity and temperature contours in this flight condition are shown in Fig. 10 and Fig. 11,

respectively. As expected, the overall temperatures are cooler compared to the initial takeoff climb flight condition due to the reduced power and the higher flight velocity. The maximum average temperature aft of the motor cooling slots is about 58.8°C, a reduction of over eight degrees Celsius in the **CM cooling** flow. A similar reduction is noted for the **CMC high-voltage cooling** flow, though only about a two-degree difference is seen in the **CMC low-voltage cooling** flow. In the latter case, the cooling flow is dominated by the ambient temperature in the air inlets and less so by the flow velocity. Also, the total energy addition in this flow path is only about 60 W total, as shown earlier in Table 4.

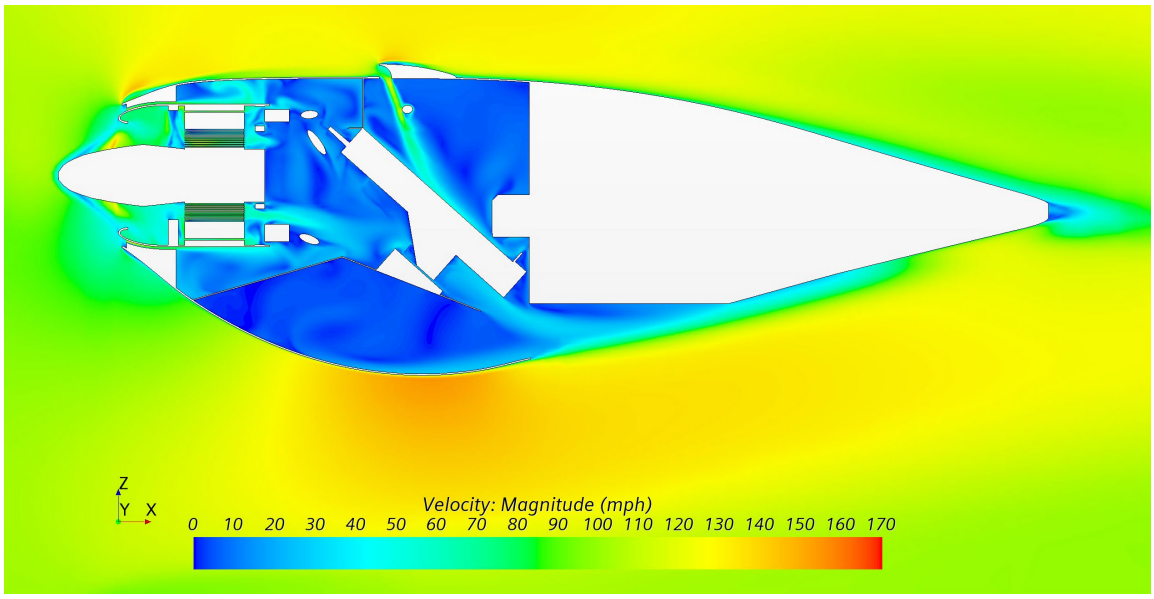

Fig. 10 Air velocity contours in the Mod II cruise nacelle for the cruise climb flight condition.

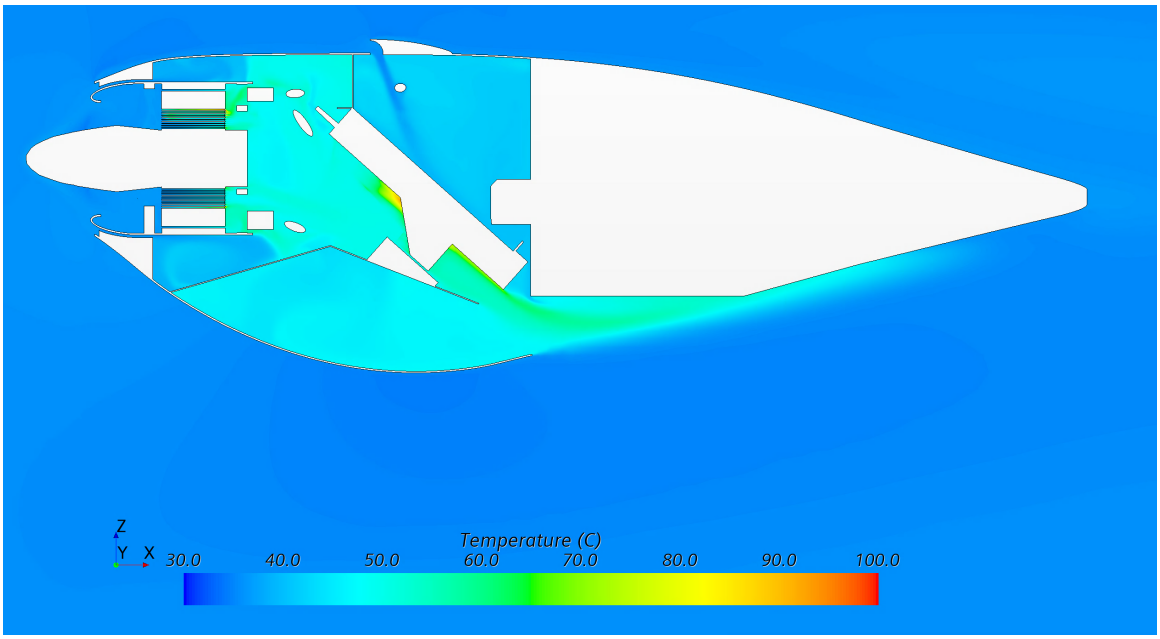

Fig. 11 Air temperature contours in the Mod II cruise nacelle for the cruise climb flight condition.

The dash flight condition represents the highest airspeed and altitude analyzed, both of which are favorable for cooling by increasing total airflow and lowering ambient temperature. However, it also represents the peak power level seen in flight (same power setting as used for the initial takeoff climb condition). This condition is not expected to yield cooling issues; however, it was considered an important condition to analyze to ensure the high velocities did

not lead to unexpected flow states. No flow anomalies were seen in the dash flight condition simulations as compared to the initial takeoff climb and cruise climb flight conditions. Two-dimensional slices of the velocity and temperature contours in this flight condition are shown in Fig. 12 and Fig. 13, respectively. As expected, the overall air temperatures are lower. The maximum temperature seen in the **CM cooling** flow is much cooler than the previous two conditions at 46°C. The **CMC low-voltage cooling** flow now sees flow velocities that exceed 100 mph; as such, this is an area where the overall dynamic loads from the air jet should be scrutinized to ensure that these loads do not cause any concerns associated with CMC mounting or other hardware in this location.

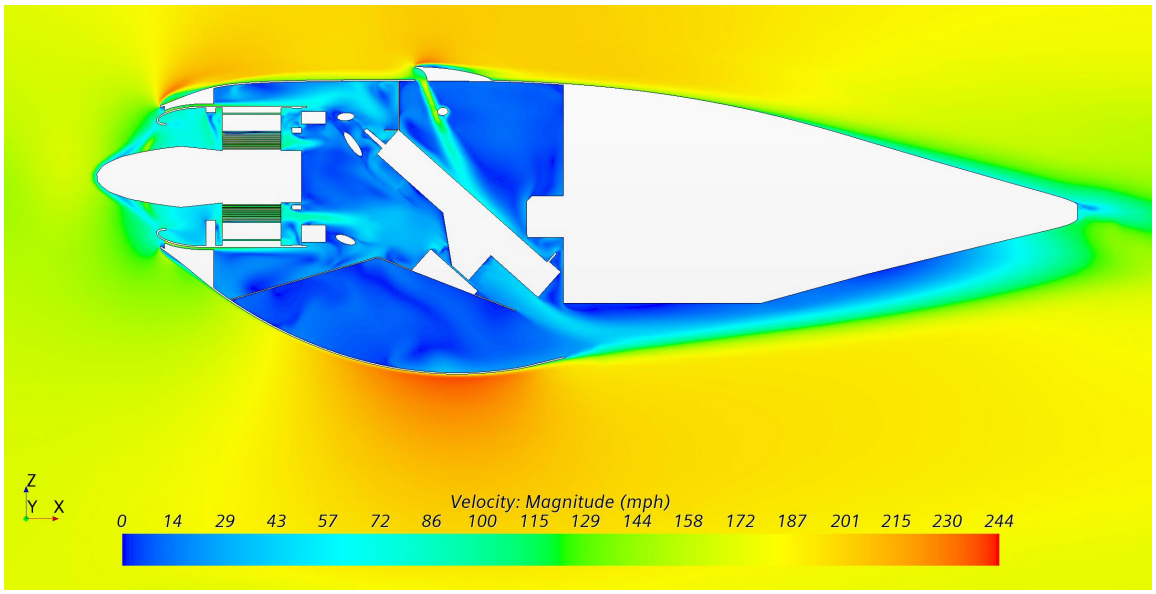

Fig. 12 Air velocity contours in the Mod II cruise nacelle for the dash flight condition.

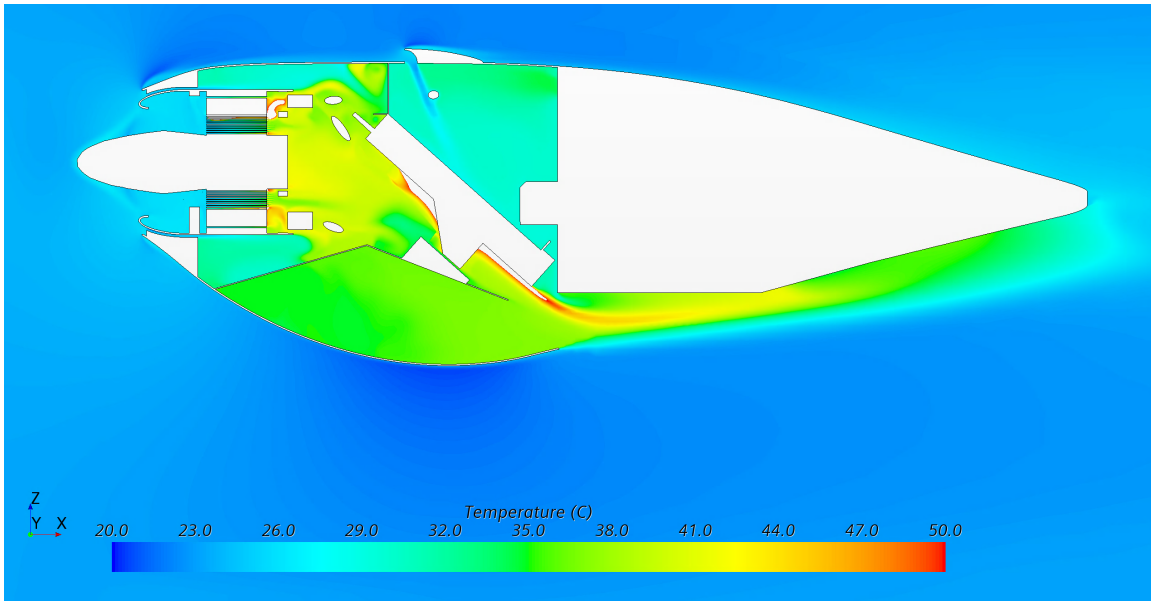

Fig. 13 Air temperature contours in the Mod II cruise nacelle for the dash flight condition.

C. Component Temperature Estimates

The CFD results provided critical data on mass flow, temperature, and velocity of local flow conditions to pass to the ICPT model. The detailed station mapping used for inputs to the ICPT components is given in Table 5. Information on the details of these station locations in the CFD model is provided in the Appendix, specifically in Fig. 14. The

flow stations in this figure are numbered in order from the nacelle inlet (station 1) through the main nacelle exhaust (station 6). Some flow stations were further subdivided, as denoted by an immediate letter a, b, or c following the station number – usually to show an inlet, midpoint, and exit to a particular station control volume. Other station descriptors follow with an underscore if needed and include "_b" for a bypass flow,[**] "_lv" for low-voltage, "_hv" for high-voltage, "_L" or "_R" for left or right, "_g" for the airgap between the rotor and stator, "_s" for the stator cooling slots, and "_e" for exhaust.

Table 5 Nacelle flow stations corresponding to ICPT inputs

Component	Input Station ID	Input Values
CM (aft) winding	2a_g, 2a_s	temperature, mass flow
CM magnet	2a_g	temperature, mass flow
CMC FET junction	5b_hv_L, 5b_hv_R	temperature, mass flow
CMC FPGA	5b_lv_L, 5b_lv_R	temperature, velocity
CMC driver board	5b_lv_L, 5b_lv_R	temperature, velocity
CMC AC/DC board	5b_lv_L, 5b_lv_R	temperature, velocity
CMC CPU board	5b_lv_L, 5b_lv_R	temperature, velocity

The flow inputs to the ICPT CM model were taken from the station at the inflow face of the CM cooling slots (station 2a), and the flow inputs to the ICPT CMC high- and low-voltage models were taken at the midstream portion of the CMC (station 5b). The CM magnet temperature in the ICPT was defined based on the CM airgap temperature in the **CM cooling** flow, so the ICPT results for magnet temperature are conservative from a cooling perspective (since the outer half of the magnets will be bathed in the cooler **CM bypass** flow). The CMC midstream value (station 5b) was selected to represent the **CMC high-voltage cooling** flow since the arrangement in the Mod II nacelle is such that mixing from the **CM cooling** flow and **CM bypass** flow is still occurring prior to the midstream location on the high-voltage side. This was viewed as more conservative for cooling estimation for the components in this flow. On the low-voltage side, the middle of the CMC station represented a point where the jet from the upper nacelle air inlets had spread out slightly, resulting in a local flow assumption that is again likely conservative from a cooling perspective.

The component temperatures were estimated by inputting the CFD-generated flow station data into the ICPT model. The resulting component temperatures, along with the additional temperature margin beyond the margined limits from Table 1, are shown in Table 6. These results show that, in almost all cases, the components remain below the margined temperature limits that were defined in accordance with the project thermal margin plan. Two exceptions are highlighted in Table 6 – the CMC AC/DC board and the CMC CPU board, both of which are located on the low-voltage side of the CMC in the **CMC low-voltage cooling** flow. They are both less than two degrees Celsius above their margined limit during the initial takeoff climb flight condition. Hence, either larger "Mickey Ear" inlets are required, or the project may need to limit the maximum allowable ambient temperature to maintain the desired temperature margins.

Table 6 Component temperatures and margins for the three flight conditions analyzed in this paper

Component	Initial T/O Climb		Cruise Climb		Dash	
	T (°C)	Additional margin (°C)	T (°C)	Additional margin (°C)	T (°C)	Additional margin (°C)
CM winding	109.4	14.6	92.2	31.8	85.6	38.4
CM magnet	45.4	37.6	43.1	39.9	31.9	51.1
CMC FET junction	104.9	45.1	91.7	58.3	85.3	64.7
CMC FPGA	75.9	13.1	73.2	15.8	58.5	30.5
CMC driver board	76.2	12.8	73.6	15.4	59.2	29.8
CMC AC/DC board	75.6	**-1.6**	73.1	0.9	58.7	15.3
CMC CPU board	75.1	**-1.1**	72.4	1.6	57.7	16.3
MDAU case	61.4	12.6	57.0	17.0	44.8	29.2
FOBE case	55.7	18.3	51.3	22.7	39.9	34.1

[**] Note that "b" refers to a mid-station location, whereas the underscore in "_b" refers to the bypass flow.

V. Summary

This document summarized the analysis approach used to evaluate the component temperatures of the cruise propulsion system components in the X-57 Mod II cruise nacelles. The analysis approach required an integrated component thermal model called the ICPT and a steady-state CFD analysis of the internal flowpath in the Mod II cruise nacelles that was used to populate the input flow conditions for the ICPT model.

The team identified three flight conditions of interest that would bound the thermal performance throughout the flight envelope – a peak power, low-speed, initial climb after takeoff; an MCP cruise climb at a higher airspeed; and a peak-power dash at high altitude and high airspeed. Of these, the peak power initial takeoff climb case was expected and shown to be the most thermally stressful condition since it involves the lowest airspeeds (and therefore lowest airflow rates through the nacelle), highest component heat rejection due to the peak motor power levels, and highest ambient air temperatures. The X-57 Project Hot Day Reference Atmosphere was the most stressful ambient environment for the three flight conditions analyzed.

A detailed CFD analysis of the three flight conditions was conducted, which verified that the takeoff and initial climb condition resulted in the worst-case flow station conditions from a cooling perspective for the CM and CMCs. In these conditions, all the electrical components in the CM and CMC other than two of the low-voltage CMC components were found to exceed the thermal margin specified in the project thermal margin requirements. These two low-voltage components were not predicted to exceed their maximum operating temperature but had approximately two degrees less margin than the 11°C required per the project thermal margin plan. This indicated that either larger auxiliary cooling inlets are needed for the low-voltage CMC cooling path, or that the project needs to reduce the maximum ambient temperature for takeoff operations by two degrees Celsius. Otherwise, the Mod II nacelle cooling flowpaths as designed are adequate for the planned flights for X-57 Mod II.

Appendix: Flow Station Properties from CFD Analysis

The detailed CFD results are indexed to the stations identified in Fig. 14. Note that the stations 0_b and 0_c are normal projections of the stations 1_b and 1_c to an upstream location far to the left of the figure in the undisturbed freestream flow and are not shown. The results for the initial takeoff climb conditions are shown in Table 7, the results for the cruise climb conditions are shown in Table 8, and the results for the dash conditions are shown in Table 9.

Acknowledgments

This work was funded by the Flight Demonstrations and Capabilities Project within the Integrated Aviation Systems Program of NASA's Aeronautics Research Mission Directorate. The authors thank NASA for their financial and technical support of this effort. The authors also wish to thank Empirical Systems Aerospace for their expertise in support of the analyses in this paper. Finally, the authors thank Sydney Schnulo (now of General Motors) for her efforts associated with the X-57 thermal analysis throughout her career at NASA.

References

[1] Borer, N. K., Patterson, M. D., Viken, J. K., Moore, M. D., Clarke, S., Redifer, M., Christie, R., Stoll, A., Dubois, A, Bevirt, J., Gibson, A., Foster, T., Osterkamp, P., "Design and Performance of the NASA SCEPTOR Distributed Electric Propulsion Flight Demonstrator," 16th AIAA Aviation Technology, Integration, and Operations Conference, AIAA AVIATION Forum, (AIAA 2016-3920), June 2016. doi: 10.2514/6.2016-3920

[2] "Armstrong Flight Research Center / Edwards Air Force Base Climatology," https://weather.dfrc.nasa.gov/Climatology, accessed 12 December 2022

[3] "Simcenter STAR-CCM+ software," Siemens, https://plm.sw.siemens.com/en-US/simcenter/fluids-thermal-simulation/star-ccm/, accessed 27 April 2023.

[4] Menter, F. R., "Two-Equation Eddy-Viscosity Turbulence Models for Engineering Applications," *AIAA Journal*, Vol. 32, No. 8, 1994, pp. 1598-1605. doi: 10.2514/3.12149

[5] Durbin, P., "On the k-3 stagnation point anomaly," *International Journal of Heat and Fluid Flow*, Vol. 17, No. 1, 1996, pp. 89-90. doi: 10.1016/0142-727X(95)00073-Y

Station	Description
0_b	freestream to bypass
0_c	freestream to core
1_b	CM bypass inlet
1_c	CM core inlet
2a_b	CM bypass just prior to plane of cooling slots
2a_g	CM rotor-stator gap just prior to plane of cooling slots
2a_s	CM cooling fin slots just prior to plane of cooling slots
2b_b	CM bypass midway through cooling slots
2b_g	CM rotor-stator gap midway through cooling slots
2b_s	CM cooling fin slots midway through cooling slots
2c_b	CM bypass at plane just after cooling slots
2c_g	CM rotor-stator gap at plane just after cooling slots
2c_s	CM cooling fin slots just at plane just after cooling slots
ME_L	Left "Mickey Ear" inlet for CMC low-voltage cooling
ME_R	Right "Mickey Ear" inlet for CMC low-voltage cooling
4_b	Lower plenum bypass around high-voltage CMC
4_e	Upper cowl exhaust - CM exhaust pressure relief
4	mixing region behind CM for bypass and core flows
5a_hv_L	High-voltage CMC flow just prior to CMC heat sink, left
5a_hv_R	High-voltage CMC flow just prior to CMC heat sink, right
5a_lv_L	Low-voltage CMC flow, plane just prior to CMC heat sink, left
5a_lv_R	Low-voltage CMC flow, plane just prior to CMC heat sink, right
5b_hv_L	High-voltage CMC flow midway through CMC heat sink, left
5b_hv_R	High-voltage CMC flow midway through CMC heat sink, right
5b_lv_L	Low-voltage CMC flow, plane midway through CMC heat sink, lef
5b_lv_R	Low-voltage CMC flow, plane midway through CMC heat sink, rig
5c_hv_L	High-voltage CMC flow just aft of CMC heat sink, left
5c_hv_R	High-voltage CMC flow just aft of CMC heat sink, right
5c_lv_L	Low-voltage CMC flow, plane just aft of CMC heat sink, left
5c_lv_R	Low-voltage CMC flow, plane just aft of CMC heat sink, right
6a	CMC & bypass flow mixing region at aft plane of CMC
6c	mixing region at nacelle exhaust plane
7	exhaust region just aft of nacelle exhaust plane

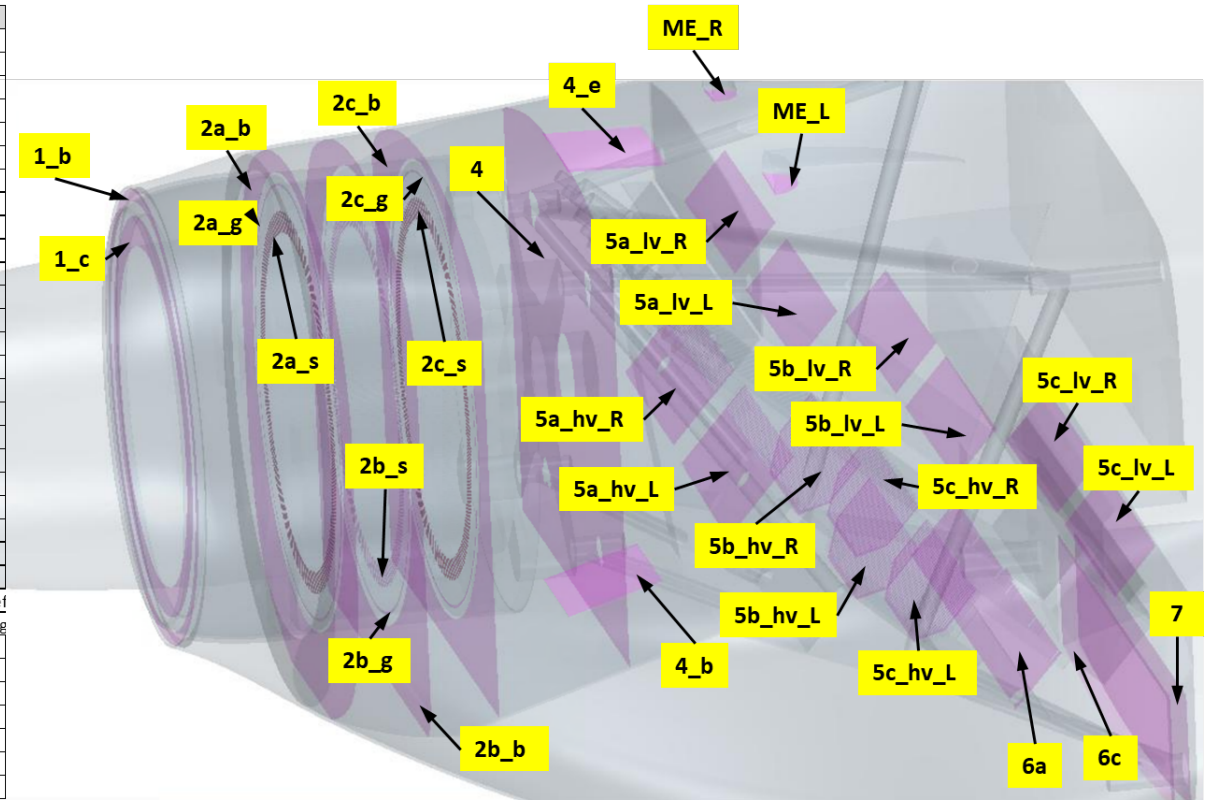

Fig. 14 CFD flow stations used to capture flow data.

Table 7 CFD results for the initial takeoff climb flight condition

Station ID	Pressure (psi)	Total Pressure (psi)	Temperature (°C)	Total Temperature (°C)	Streamwise Velocity (ft/s)	Mass Flow Rate (lbm/s)
0_b	13.41	13.53	35.85	36.61	126.4	0.959
0_c	13.41	13.53	35.85	36.61	126.4	1.794
1_b	13.55	13.61	36.28	36.66	30.5	0.234
1_c	13.54	13.66	35.87	36.66	39.1	0.560
2a_b	13.42	13.44	39.43	39.54	5.6	0.237
2a_g	13.47	13.56	38.00	38.63	67.6	0.100
2a_s	13.45	13.51	43.09	43.50	68.8	0.458
2b_b	13.42	13.43	39.60	39.69	5.0	0.235
2b_g	13.45	13.54	46.37	46.96	70.9	0.102
2b_s	13.44	13.48	54.49	54.79	71.3	0.458
2c_b	13.43	13.44	42.73	42.82	5.5	0.235
2c_g	13.43	13.51	53.42	53.99	72.5	0.102
2c_s	13.41	13.46	67.24	67.54	74.0	0.459
ME_L	13.42	13.51	37.18	37.76	87.9	0.049
ME_R	13.43	13.56	37.14	37.93	103.7	0.054
4_b	13.41	13.43	53.45	53.60	38.5	0.226
4_e	13.42	13.43	51.09	51.22	26.6	0.139
4	13.43	13.43	52.03	52.06	8.0	0.751
5a_hv_L	13.43	13.43	59.20	59.21	8.6	0.076
5a_hv_R	13.43	13.43	54.51	54.53	10.6	0.088
5a_lv_L	13.39	13.40	44.29	44.31	5.4	0.036
5a_lv_R	13.39	13.40	46.53	46.55	4.4	0.029
5b_hv_L	13.40	13.42	59.40	59.52	46.2	0.219
5b_hv_R	13.40	13.42	57.92	58.03	44.4	0.209
5b_lv_L	13.39	13.40	42.73	42.77	17.4	0.115
5b_lv_R	13.39	13.40	44.31	44.35	17.3	0.114
5c_hv_L	13.39	13.41	62.10	62.21	46.4	0.218
5c_hv_R	13.39	13.41	61.16	61.26	44.6	0.209
5c_lv_L	13.40	13.40	41.10	41.12	2.7	0.018
5c_lv_R	13.40	13.41	43.00	43.04	4.5	0.029
6a	13.40	13.40	60.09	60.13	22.9	0.422
6c	13.39	13.40	54.40	54.44	26.7	0.756
7	13.39	13.40	54.28	54.32	27.4	0.779

Table 8 CFD results for the cruise climb flight condition

Station ID	Pressure (psi)	Total Pressure (psi)	Temperature (°C)	Total Temperatures (°C)	Streamwise Velocity (ft/s)	Mass Flow Rate (lbm/s)
0_b	13.41	13.57	35.85	36.86	146.8	1.114
0_c	13.41	13.57	35.85	36.86	146.8	2.083
1_b	13.58	13.63	36.58	36.90	33.1	0.254
1_c	13.56	13.67	36.15	36.88	42.9	0.615
2a_b	13.42	13.43	39.61	39.68	6.1	0.259
2a_g	13.47	13.57	37.62	38.26	74.1	0.110
2a_s	13.45	13.52	41.49	41.96	75.5	0.503
2b_b	13.42	13.43	39.88	39.94	5.5	0.257
2b_g	13.45	13.54	43.87	44.47	77.2	0.112
2b_s	13.43	13.48	49.88	50.22	77.6	0.503
2c_b	13.42	13.43	39.91	39.97	5.9	0.255
2c_g	13.43	13.52	49.03	49.64	78.7	0.112
2c_s	13.41	13.46	58.83	59.17	79.9	0.504
ME_L	13.43	13.53	37.22	37.89	93.9	0.052
ME_R	13.43	13.56	37.18	38.01	106.0	0.055
4_b	13.40	13.43	48.52	48.71	37.5	0.237
4_e	13.40	13.43	48.50	48.68	37.9	0.199
4	13.42	13.43	47.64	47.67	8.7	0.830
5a_hv_L	13.42	13.42	55.87	55.89	8.9	0.080
5a_hv_R	13.42	13.43	52.78	52.79	9.2	0.077
5a_lv_L	13.39	13.39	42.79	42.81	5.7	0.038
5a_lv_R	13.39	13.39	44.13	44.16	4.8	0.032
5b_hv_L	13.40	13.41	53.67	53.79	46.2	0.222
5b_hv_R	13.40	13.41	52.75	52.86	44.0	0.211
5b_lv_L	13.39	13.40	41.32	41.36	18.2	0.121
5b_lv_R	13.39	13.40	42.23	42.28	18.6	0.123
5c_hv_L	13.39	13.41	55.99	56.10	46.2	0.221
5c_hv_R	13.39	13.41	55.33	55.43	44.2	0.210
5c_lv_L	13.40	13.40	40.47	40.50	2.7	0.018
5c_lv_R	13.40	13.40	41.61	41.65	4.9	0.032
6a	13.39	13.40	54.41	54.45	22.8	0.427
6c	13.39	13.40	50.07	50.11	27.0	0.776
7	13.39	13.40	49.90	49.95	27.8	0.799

Table 9 CFD results for the dash flight condition

Station ID	Pressure (psi)	Total Pressure (psi)	Temperature (°C)	Total Temperatures (°C)	Streamwise Velocity (ft/s)	Mass Flow Rate (lbm/s)
0_b	10.91	11.30	23.25	26.23	253.5	1.631
0_c	10.91	11.30	23.25	26.23	253.5	3.051
1_b	11.29	11.34	25.91	26.29	53.0	0.349
1_c	11.19	11.32	25.34	26.26	66.3	0.813
2a_b	10.93	10.95	30.84	30.96	9.9	0.357
2a_g	11.02	11.16	26.54	27.58	115.7	0.146
2a_s	10.98	11.12	29.92	30.99	117.5	0.665
2b_b	10.93	10.94	30.56	30.65	9.0	0.355
2b_g	10.98	11.11	32.63	33.64	121.4	0.150
2b_s	10.96	11.06	37.62	38.43	121.1	0.665
2c_b	10.93	10.94	30.39	30.49	9.7	0.353
2c_g	10.94	11.07	37.45	38.47	124.3	0.150
2c_s	10.91	11.01	45.96	46.79	124.9	0.666
ME_L	10.95	11.14	25.49	26.94	138.3	0.065
ME_R	10.96	11.18	25.45	27.09	145.7	0.065
4_b	10.91	10.95	37.61	37.95	50.5	0.273
4_e	10.87	10.94	36.16	36.74	79.6	0.351
4	10.94	10.95	36.15	36.23	13.9	1.112
5a_hv_L	10.94	10.95	41.44	41.49	13.6	0.103
5a_hv_R	10.94	10.95	38.97	39.01	14.7	0.104
5a_lv_L	10.89	10.90	30.66	30.71	10.5	0.059
5a_lv_R	10.89	10.90	31.81	31.87	8.9	0.049
5b_hv_L	10.90	10.93	41.74	41.98	66.0	0.268
5b_hv_R	10.90	10.93	40.96	41.20	66.2	0.268
5b_lv_L	10.89	10.90	29.97	30.04	25.9	0.145
5b_lv_R	10.89	10.90	30.49	30.59	27.8	0.155
5c_hv_L	10.89	10.92	43.98	44.20	66.0	0.266
5c_hv_R	10.89	10.92	43.41	43.64	66.4	0.267
5c_lv_L	10.90	10.90	29.48	29.54	3.8	0.021
5c_lv_R	10.90	10.91	30.20	30.27	6.2	0.035
6a	10.90	10.91	42.82	42.92	33.2	0.526
6c	10.89	10.90	38.79	38.89	38.7	0.938
7	10.89	10.90	38.71	38.81	39.5	0.958